

Targeting distinct myeloid cell populations in vivo using polymers, liposomes and microbubbles



Can Ergen ^{a,1}, Felix Heymann ^{a,1}, Wa'el Al Rawashdeh ^b, Felix Gremse ^b, Matthias Bartneck ^a, Ulf Panzer ^c, Robert Pola ^d, Michal Pechar ^d, Gert Storm ^{e,f}, Nicole Mohr ^g, Matthias Barz ^g, Rudolf Zentel ^g, Fabian Kiessling ^b, Christian Trautwein ^a, Twan Lammers ^{b,e,f,**}, Frank Tacke ^{a,*}

^a Department of Medicine III, University Hospital Aachen, Aachen, Germany

^b Department of Experimental Molecular Imaging, University Clinic and Helmholtz Institute for Biomedical Engineering, RWTH Aachen University, Aachen, Germany

^c Department of Medicine III, University Hospital Hamburg-Eppendorf, Hamburg, Germany

^d Institute of Macromolecular Chemistry, Academy of Sciences of the Czech Republic, Prague, Czechia

^e Department of Pharmaceutics, Utrecht Institute for Pharmaceutical Sciences, Utrecht University, Utrecht, The Netherlands

^f Department of Targeted Therapeutics, MIRA Institute for Biomedical Technology and Technical Medicine, University of Twente, Enschede, The Netherlands

^g Institute of Organic Chemistry, Johannes Gutenberg University, Mainz, Germany

ARTICLE INFO

Article history:

Received 12 September 2016

Received in revised form

20 October 2016

Accepted 7 November 2016

Available online 9 November 2016

Keywords:

Targeted delivery

Nanomedicine

Macrophages

Polymers

Liposomes

Microbubbles

ABSTRACT

Identifying intended or accidental cellular targets for drug delivery systems is highly relevant for evaluating therapeutic and toxic effects. However, limited knowledge exists on the distribution of nano- and micrometer-sized carrier systems at the cellular level in different organs. We hypothesized that clinically relevant carrier materials, differing in composition and size, are able to target distinct myeloid cell subsets that control inflammatory processes, such as macrophages, neutrophils, monocytes and dendritic cells. Therefore, we analyzed the biodistribution and in vivo cellular uptake of intravenously injected poly(*N*-(2-hydroxypropyl) methacrylamide) polymers, PEGylated liposomes and poly(butyl cyanoacrylate) microbubbles in mice, using whole-body imaging (computed tomography - fluorescence-mediated tomography), intra-organ imaging (intravital multi-photon microscopy) and cellular analysis (flow cytometry of blood, liver, spleen, lung and kidney). While the three carrier materials shared accumulation in tissue macrophages in liver and spleen, they notably differed in uptake by other myeloid subsets. Kupffer cells and splenic red pulp macrophages rapidly take up microbubbles. Liposomes efficiently reach dendritic cells in liver, lung and kidney. Polymers exhibit the longest circulation half-life and target endothelial cells in the liver, neutrophils and alveolar macrophages. The identification of such previously unrecognized target cell populations might open up new avenues for more efficient drug delivery.

© 2016 Elsevier Ltd. All rights reserved.

1. Introduction

Over the years, numerous drug delivery systems have been

* Corresponding author.

** Corresponding author. Department of Experimental Molecular Imaging, University Clinic and Helmholtz Institute for Biomedical Engineering, RWTH Aachen University, Aachen, Germany.

E-mail addresses: tlammers@ukaachen.de (T. Lammers), frank.tacke@gmx.net (F. Tacke).

¹ These authors contributed equally to this work.

evaluated in an effort to optimize therapeutic efficacy and reduce side effects [1–3]. However, the translation of novel drug delivery systems into clinical settings remains challenging. A major obstacle to date is to understand how new biomaterials are processed by cells in vivo and to which extent they target and modulate immune cells in various tissues. In evaluating the biodistribution of drug carrier systems, techniques like whole-body imaging and histological evaluation have been widely employed to assess their potential for targeted therapeutic applications [4–7]. These techniques usually depend on a high density of the studied cell populations targeted by the carriers to allow quantification of their

uptake, thereby implying the chance of not detecting relevant cellular targets. Importantly, basic and clinical immunological research has demonstrated that different cell populations with only a small contribution to the total number of leukocytes can be highly relevant for diseases through regulating the behavior of other immune cells [8–10]. Specifically, this applies to the heterogeneous population of myeloid cells (comprising neutrophils as well as monocyte, macrophage and dendritic cell (DC) subsets) because these components of innate immunity largely control inflammatory processes. For instance, liver phagocytes can rapidly release inflammatory mediators (e.g. cytokines, reactive oxygen species and chemokines), which may initiate tissue injury and trigger immune cell infiltration, while tumor-associated macrophages oftentimes suppress T cell responses against cancer [10]. Targeting these myeloid cell types using nanomedicine formulations and micro-carrier materials might therefore bear a potential risk for unintentional off-target effects as well as a novel opportunity for treating autoimmune diseases and cancer.

It has been shown that the mononuclear phagocytic system is responsible for the clearance of nanoparticles and microparticles [11]. Carriers below 6–8 nm in diameter are renally excreted [12], while larger materials show a tendency to be taken up in liver, spleen and bone marrow [13,14]. Microsized carriers are also taken up in the lung [13]. Two factors have a general role for cellular biodistribution: Firstly, carriers that are injected intravenously need to cross the endothelium and traverse the interstitial space to interact with tissue macrophages [15]. Secondly, factors like surface charge, radius of curvature or protein opsonization are important for the cellular interactions of drug delivery systems [16].

It was suggested that macrophages showed the highest uptake level followed by DC and monocytes [13,17]. The analysis of cellular biodistribution performed for immune organs showed time- and organ-dependent differences in cellular biodistribution of polystyrene nanoparticles [18]. However, a systematic approach analyzing the uptake by distinct subsets of myeloid cells including organ-resident macrophages in different parenchymal organs in the same animal has been lacking. In this study, we aim to provide a holistic understanding of the biodistribution ranging from whole-body to organ to single cell level of three clinically relevant drug delivery systems: polymeric macromolecules (poly(*N*-(2-hydroxypropyl) methacrylamide; 10 nm) [19–21], PEGylated liposomes (100 nm) [22,23] and poly(butyl cyanoacrylate)-based microbubbles (2 μ m) [24,25]. These carriers show differences in various properties including composition, size and surface properties, which all influence biodistribution and cellular uptake. The primary aim of this study was to provide a better understanding of the cellular biodistribution of these three systems, for which many preclinical and clinical applications have been reported. This knowledge can be used as a starting point for developing systems and strategies for targeting specific cell types in specific organs. To systematically and quantitatively determine biodistribution, we used a multicolor flow cytometry-based approach to distinguish 20 different myeloid cells in different organs as well as 20 different lymphoid cells in blood, kidney, liver, lung and spleen. In addition, we employed real-time two-photon laser scanning microscopy (TPLSM) to assess the intrahepatic biodistribution in order to monitor early uptake [26,27], and computed tomography - fluorescence-mediated tomography (CT-FMT) to relate these findings to whole-body biodistribution and organ uptake [6,28].

2. Results and discussion

To better understand the biodistribution of clinically relevant nano- and microcarrier materials, we employed fluorescently labeled pHPPMA polymers (10 nm), PEGylated liposomes (100 nm)

and PBCA-based microbubbles (2 μ m) (Fig. 1). Labeling the carriers with an infrared fluorophore used for whole body-imaging (μ CT-FMT) and a fluorophore excitable by visible light used for flow cytometry and microscopy allowed imaging of carrier biodistribution on the various scales. Dual labeling is necessary, because there are no commercial flow cytometers that allow the detection of infrared fluorophores, and μ CT-FMT is most accurate with fluorophores excited by 750 nm [29]. Fluorophore labeling allowed imaging of carrier biodistribution using whole-body imaging (μ CT-FMT) as well as flow cytometry and microscopy. Intravital TPLSM of the liver was performed during the first 2 h after carrier injection and *ex vivo* TPLSM was performed 14 h after carrier injection. At three different time points (4 h, 14 h and 120 h after carrier injection), extensive flow cytometric analyses were performed to address the single cell types relevant for carrier clearance in different parenchymal organs (liver, spleen, lung and kidney) as well as blood (Fig. 1).

2.1. Temporal and spatial differences in organ accumulation of carrier materials

Optical imaging has been extensively used to monitor nano/micro-carrier biodistribution *in vivo* [20]. In this study, we applied μ CT-FMT in hairless immunocompetent mice (SKH1-e) [30], to assess the whole-body distribution of polymers, liposomes and microbubbles. We segmented different organs based on μ CT scans and determined carrier accumulation (Fig. 2A). Circulation times were assessed using the signal in the segmented cardiac region. The blood half-life was short for microbubbles (80% reduction of total blood signal after 4 h) [5]. However, it was prolonged for PEGylated liposomes (80% reduction of total blood signal after 24 h) [5,31] and for polymers (80% reduction of total blood signal after 120 h; Fig. 2B) [32].

The liver was the organ with the highest uptake (for all carriers approximately 30%ID). In the lung, microbubbles show an initial signal peak (3% ID after 15 min) that rapidly decreased to a steady signal of 0.7% ID after 8 h. This is in line with the accumulation of microbubbles in the lung capillary system [5] that are either resolved by cellular uptake or are resolved by disassembly leading to their redistribution and thereby a fast signal decrease within the first hours. Liposomes accumulated in the lung 4 h after injection. Polymers and liposomes showed a stable signal as high as 2% ID in the kidney up to 48 h after injection, and both show urinary secretion.

Using μ CT-FMT we could show that the carriers used in this study are suitable to target various organs such as liver, spleen, lung, and kidney with divergent specificity in line with previous studies [5,19,33], therefore rendering them suitable for further investigating their potential use as prototypic drug delivery systems for targeted therapies.

2.2. Intravital TPLSM imaging of carrier uptake kinetics by liver phagocytes

Intravital TPLSM allows real-time assessment of carrier distribution at the target site, thereby providing complementary information to the other methods employed, which only allow “snapshots” of the *in vivo* situation at selected time points. To this end, we performed intravital TPLSM scans of the liver over several hours to monitor the kinetics of carrier biodistribution [34]. The liver was chosen as a primary target organ because of the pronounced accumulation of all carrier materials (as verified in the μ CT-FMT scans) [35].

Latex microspheres (0.5 μ m) were injected 2 h prior to imaging to label liver resident macrophages (i.e. Kupffer cells). In a recent

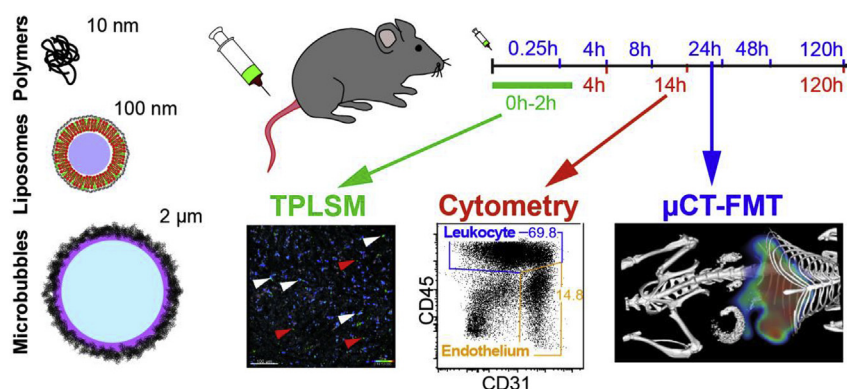


Fig. 1. Study design. Healthy mice were intravenously injected with fluorescently labeled polymers, liposomes or microbubbles. After carrier injection, biodistribution in mice was assessed using a multiscale imaging approach. Hybrid computed tomography - fluorescence-mediated tomography (μ CT-FMT) was performed at different time points after i.v. administration to monitor the organ distribution kinetics of the carrier materials. Flow cytometry was performed at 4, 14 and 120 h after carrier injection to track the single cell dynamics of carrier biodistribution. Intravital two-photon microscopy (TPLSM) was performed directly before particle injection up until 2 h after injection to monitor the short-term dynamics of carrier biodistribution in the liver.

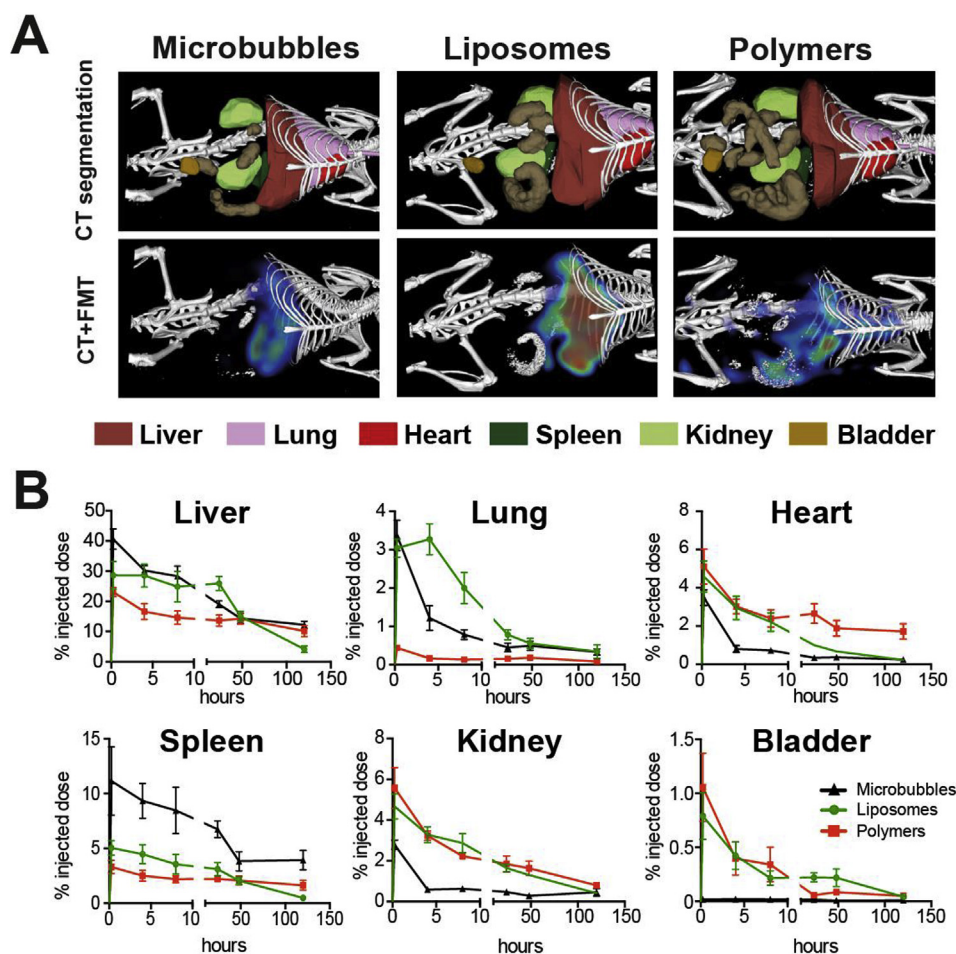


Fig. 2. Whole-body imaging of the carriers by μ CT-FMT. (A) FMT was coregistered with μ CT. The upper images show an overlay of μ CT images with the organ segmentation, while the lower images show an overlay of the FMT signal 24 h after carrier injection with the μ CT images. Microbubbles showed a high signal in liver and spleen. Liposomes accumulated in the liver and polymers were still apparent in the heart. Legend shows the color-code of the respect organ (B) Imaging was performed 15 min, 4, 8, 24, 48 and 120 h after injection and the signal is shown for the six organs segmented. The highest signal was visible in the liver. Microbubbles accumulated in the spleen, while liposomes and polymers show a longer half-life and showed higher renal values. Data shown are derived from $n = 5$ animals per condition.

study, we could show specific labeling of professional phagocytes using these microspheres without apparent alteration of immune cell function [36]. The different types of carriers were injected

through an intracardiac right ventricular catheter 2 min after starting the imaging procedure. To quantify the contribution of the different cellular compartments to nano- and microcarrier

distribution, we segmented two of them (first: vasculature, consisting of intrahepatic blood as well as endothelial cells, and second: Kupffer cells) in the liver using a voxel-based approach.

Microbubbles entering the liver were rapidly and almost exclusively removed from circulation by latex microsphere-positive Kupffer cells within the first 30 min, thereby clearing all larger blood vessels from the carrier (Fig. 3A–B, Suppl. Video 1), except for singular agglomerates of microbubbles traversing vessels, which were likely monocytes carrying microbubbles. This underlines the strong capability of Kupffer cells to clear the blood from micro-particles [37].

Supplementary video related to this article can be found at <http://dx.doi.org/10.1016/j.biomaterials.2016.11.009>.

Liposome injections initially led to a strong intravascular signal with a gradual and constant hepatic accumulation of the carriers within the next 2 h, targeting Kupffer cells and endothelial cells (lining small sinusoids) (Fig. 3A–B, Suppl. Video 2). Some vessels showed liposome uptake by endothelial cells indicated by strong fluorescent signals 2 h after injection. The carriers inside the vessels, where no apparent uptake by endothelial cells was visible, showed no significant decline of intravascular signal during the course of the experiment, which was also in accordance to the prolonged blood half-life observed in μ CT-FMT. Fluorescent cells passing through sinusoids were also observed (Suppl. Video 2) and showed a similar pattern as patrolling leukocytes traversing the liver sinusoids [36].

Supplementary video related to this article can be found at <http://dx.doi.org/10.1016/j.biomaterials.2016.11.009>.

Polymers remained mostly inside the vasculature during the imaging period, showing only minor uptake by endothelial cells (Fig. 3A–B, Suppl. Video 3). Uptake by Kupffer cells was also significantly lower compared to the other carriers, but was visible

as early as 10 min after injection. Free polymers evoked a stable and diffuse intravascular signal over several hours.

Supplementary video related to this article can be found at <http://dx.doi.org/10.1016/j.biomaterials.2016.11.009>.

Intravital TPLSM could thereby show that uptake by Kupffer cells well as blood leukocytes is highly relevant for the bio-distribution of microbubbles and liposomes, already within minutes to hours after systemic administration. Liposomes and polymers showed a prolonged high intravascular signal and a targeting of liver endothelial cells, while this behavior was not apparent after the injection of microbubbles.

2.3. Distinct pattern of myeloid cell targeting in blood

While intravital TPLSM indicated that blood leukocytes could take up all three carrier materials, this effect was most prominent for liposomes. We therefore characterized carrier uptake by circulating cells looking at granulocytes ($CD11b^{hi}Ly-6G^{hi}$) as well as $Ly-6C^{hi}$ and $Ly-6C^{lo}$ monocytes ($CD11b^{+}Ly-6G^{neg}Ly-6C^{+/-}$) (Fig. 4A and Suppl. Fig. 1). These targeting properties are highly relevant since previous studies have suggested blood myeloid cell targeting for delivering drugs to tumors and inflamed tissue [38,39].

Carrier uptake was analyzed using flow cytometry, where all cells that took up the carriers show a distinct peak making it feasible to quantify the number of carrier-positive cells (Fig. 4B). Microbubbles were most efficiently taken up by $Ly-6C^{lo}$ monocytes (6.2% positive at 4 h and 1.2% after 120 h, Fig. 4B–C). The decrease in particle positive $Ly-6C^{lo}$ monocytes over time can be explained by their circulation life-time which is about 2.2 days [40], which fits to the reduction of 80% positive cells between 14 and 120 h. In contrast to microbubbles, liposomes targeted both $Ly-6C^{hi}$ and $Ly-6C^{lo}$ monocytes with almost similar efficiency. However, after 120 h

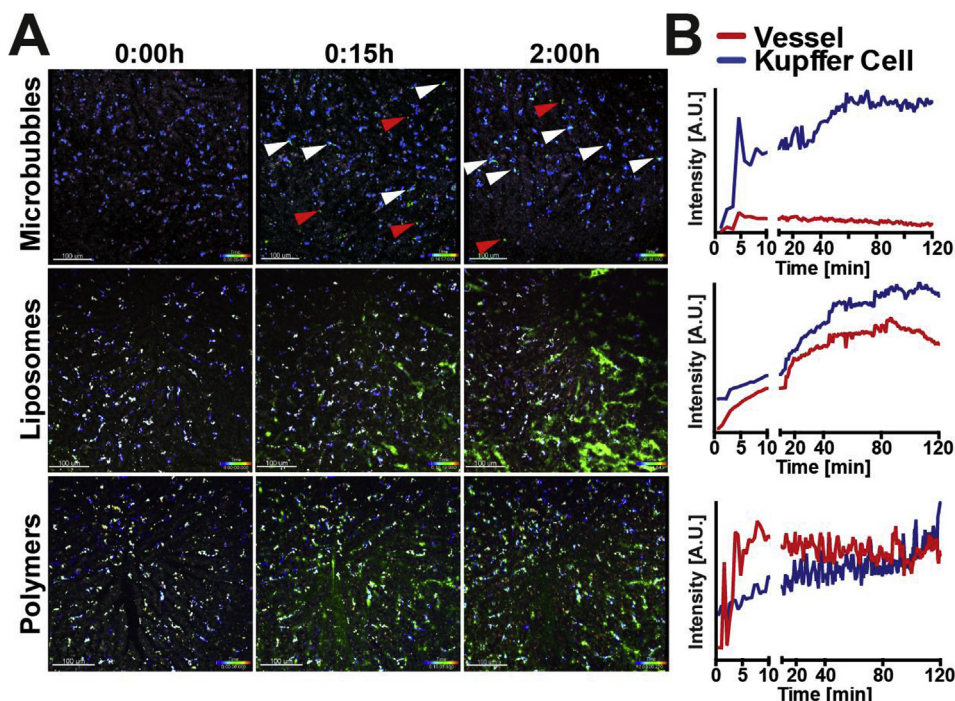


Fig. 3. Real-time distribution of nano- and microcarriers in the liver using intravital TPLSM. (A) Representative snapshots before injection, 15 min after injection and 2 h after injection are shown (Suppl. Video 1–3). All carriers are shown in green, White arrows indicate stationary microbubbles while red arrows indicate mobile microbubbles. Microbubbles tend to accumulate close to latex-positive macrophages (blue) after 15 min. After 2 h almost all microbubbles are stationary. Upon liposome and polymer administration, an intravascular signal is visible for 15 min. While the intravascular signal stays high, carriers colocalize with latex-positive macrophages (blue) 2 h after injection. (B) The quantitative analysis of carrier distribution was performed for the vasculature (endothelium and blood, red line) as well as Kupffer cells (blue line) and the fluorescence intensity is plotted over 120 min. (For interpretation of the references to colour in this figure legend, the reader is referred to the web version of this article.)

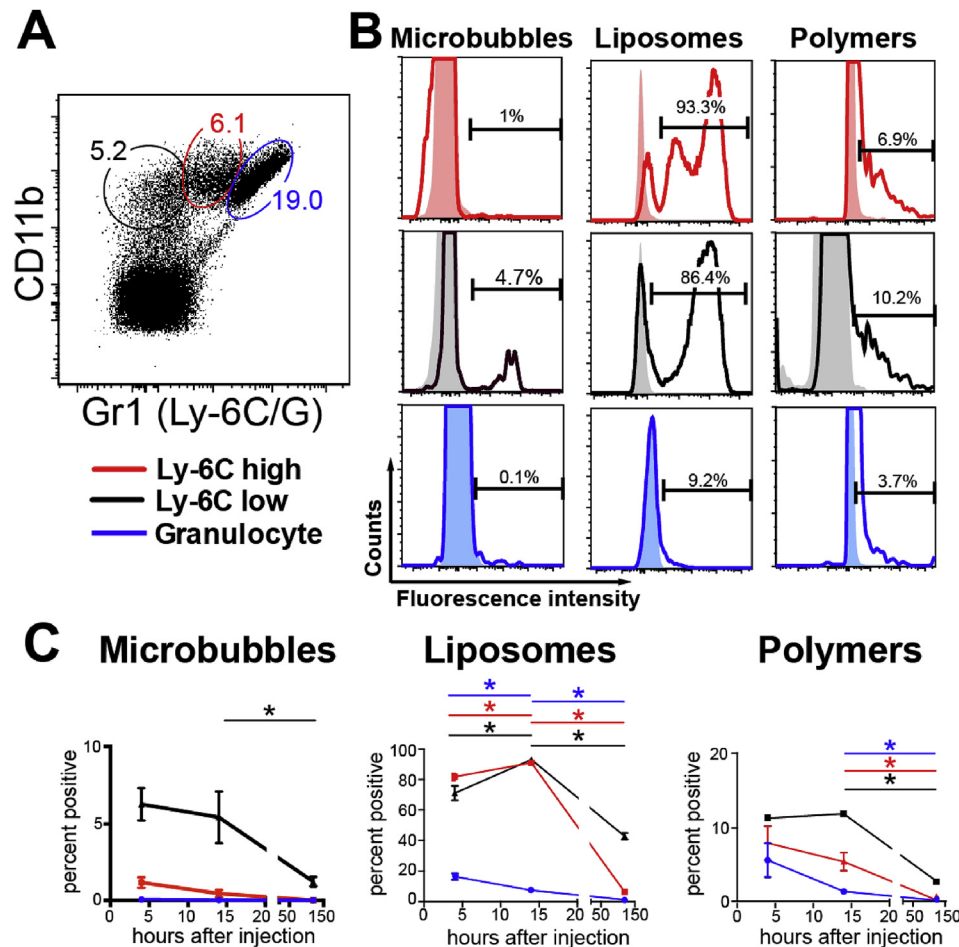


Fig. 4. Nano- and microcarrier accumulation in circulating myeloid immune cell populations. (A) Granulocytes were identified as CD11b⁺ Ly-6C^{hi} SSC^{lo-int}. Blood monocytes (CD11b⁺ SSC^{lo-int}) were further subdivided based on Ly-6C expression. (B) The signal in flow cytometry is shown as a histogram without (filled areas) and with (14 h after injection, lines) injection of each carrier; histogram gates show the ratio of carrier-positive cells. Ly-6C^{lo} monocytes took up all three carriers, while Ly-6C^{hi} monocytes only took up liposomes. Negative histogram peaks are cropped to also visualize low numbers of carrier-positive cells. (C) The carrier distribution (indicated as percent positive cells in the subset) was measured 4, 14 and 120 h after injection; significance is shown for neighboring time points. This shows that liposomes accumulate at later time points, while the highest number of carrier positive cells is reached 4 h after polymer and microbubble injection. **P* < 0.05.

there were no carrier-positive Ly6C^{hi} monocytes detectable in the circulation, presumably due to their shorter half-life in blood [40] and their conversion into Ly-6C^{lo} monocytes [41] (Fig. 4B–C). For polymers, similar to microbubbles, Ly-6C^{lo} monocytes (10.0% after 14 h) were the major population responsible for uptake, while the number of Ly-6C^{hi} monocytes (6.9%) and granulocytes (3.7%) carrying polymers was higher compared to microbubbles.

Because Ly-6C^{hi} and Ly-6C^{lo} monocytes have different roles in inflammation [42], knowledge of the carrier targeting properties are essential for using them for anti-inflammatory treatments. Liposomes were the only particles leading to a high uptake in both Ly-6C^{hi} and Ly-6C^{lo} monocytes, which is in accordance to the observation that both cell types can take up nanomedical formulations [13,23,38], while microbubbles and polymers were only taken up by Ly-6C^{lo} monocytes that have a higher intrinsic phagocytic capacity than Ly-6C^{hi} monocytes [41]. In addition, targeting of Ly-6C^{hi} monocytes has been shown to be effective in tumor therapies, because these cells actively penetrate the tumor and can be hijacked for pharmacodelivery [38]. It remains to be determined whether this mechanism is essential for the beneficial effect of liposomes in other disease models, like rheumatoid arthritis [43] or acute immune-mediated hepatitis [23].

2.4. Assessment of intrahepatic carrier biodistribution

Differential contributions of nano- and microcarrier clearance by endothelial cells and Kupffer cells were visible in intravital TPLSM. To quantify the carrier uptake by different cell types, we examined liver non-parenchymal cells using flow cytometry. In addition to Kupffer cells, we also addressed carrier uptake by other hepatic myeloid cells, such as DC and monocyte-derived macrophages (MoMF). *Ex vivo* TPLSM was used to confirm the findings of intravital TPLSM at a later time point (14 h after injection). In accordance with early time points, TPLSM showed uptake of polymers and liposomes in liver endothelial cells, albeit polymers were more efficient in that respect. All three carrier materials showed colocalization with latex-microsphere positive Kupffer cells (Fig. 5A). Cryosections showed high density for liposomes compared to the other carriers (Suppl. Fig. 2).

In accordance to *ex vivo* TPLSM, flow cytometry confirmed that polymers targeted endothelial cells (CD31⁺CD45⁺) most efficiently (Fig. 5C). In agreement to previous studies [44,45], liposomes were also partially seen in liver endothelium, albeit with a lower uptake rate of only around 3% of the endothelial cells. Liver endothelial cells differ from other endothelial cells, as they have been shown to actively sample the blood stream by macropinocytosis and

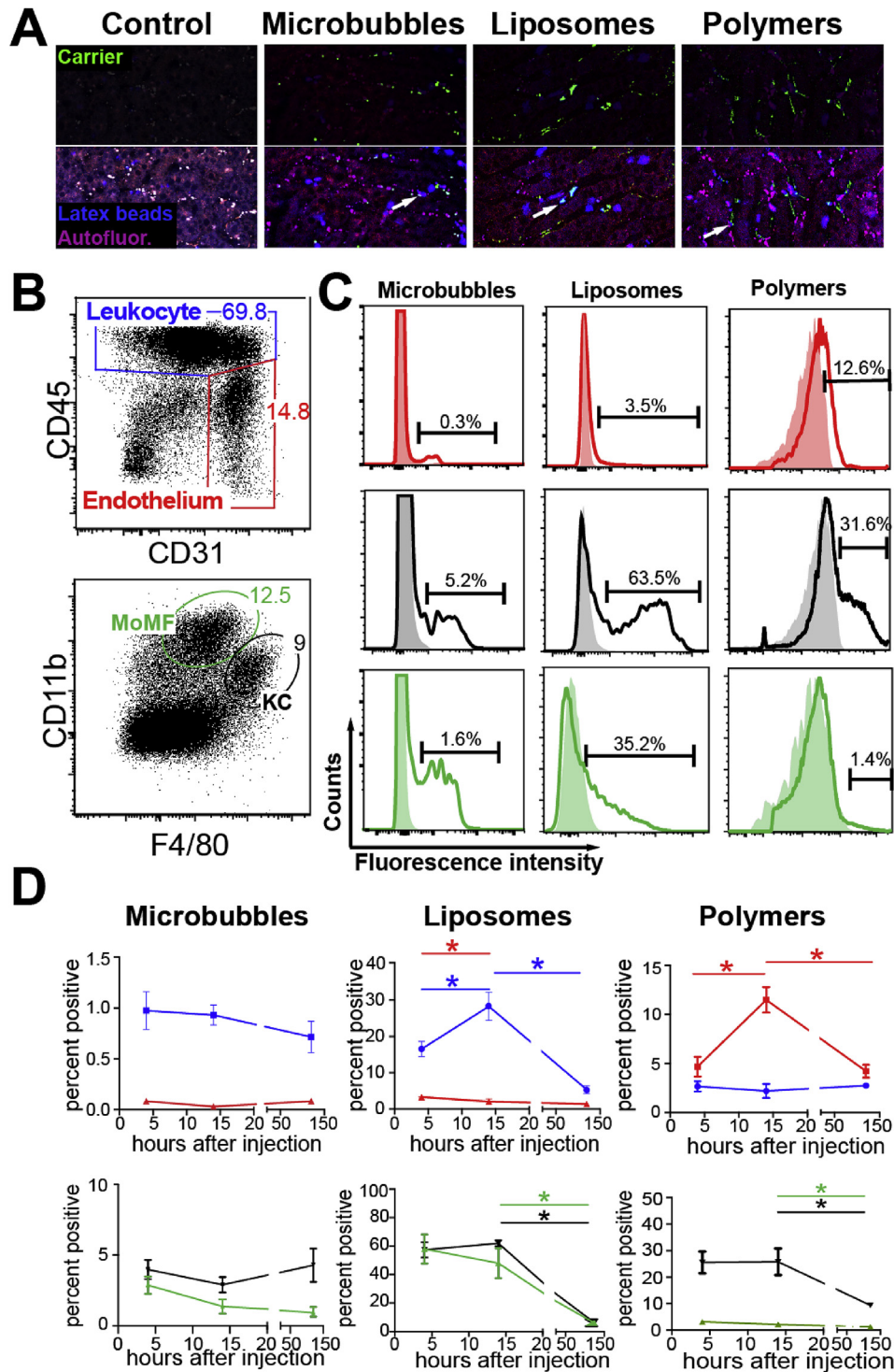


Fig. 5. Nano- and microcarrier accumulation in hepatic cell subsets. (A) The top part of the images shows the carrier signal 14 h after injection only, the lower part an overlay of fluorescent latex beads (blue) and tissue autofluorescence (orange). Arrows indicate representative cells with colocalization of carriers (in green) with latex microspheres (in blue). All three carriers show colocalization with Kupffer cells (blue) and liposomes and polymers show a stretched out perivascular signal (endothelial cells). (B) Endothelial cells were defined as CD45⁺ CD31⁺ in flow cytometry (lower right gate) and leukocytes as CD45⁺ cells (upper gate). Kupffer cells were gated as F4/80⁺CD11b^{int}, and monocyte-derived macrophages were defined as F4/80^{int}CD11b⁺. (C) The signal in flow cytometry is shown as a histogram without (filled areas) and with (14 h after injection, lines) injection of each carrier; histogram gates show the ratio of carrier-positive cells. Kupffer cells took up all three carriers, while endothelial cells only took up polymers to a major extent. Negative histogram peaks are cropped to visualize also low numbers of carrier-positive cells. (D) The carrier distribution (indicated as percent positive cells in the subset) was measured 4, 14 and 120 h after injection; significance is shown for neighboring time points. This shows a stable signal for microbubbles as well as polymers, while the liposome signal decreased over time. * $P < 0.05$. (For interpretation of the references to colour in this figure legend, the reader is referred to the web version of this article.)

receptor-mediated endocytosis [46] and shape immune responses by influencing monocyte or T-cell recruitment and differentiation [47].

Liver myeloid cells were analyzed using flow cytometry defining Kupffer cells as $CD11b^{int}F4/80^{hi}$ and MoMF as $CD11b^{hi}F4/80^{lo-int}$ (Fig. 5B and Suppl. Fig. 3). Kupffer cells showed the highest uptake for the three carriers compared to all other intrahepatic cells (Fig. 5C–D). Surprisingly, MoMF showed a lower uptake of all three particles compared to $Ly-6C^{lo}$ monocytes in blood, even though this population consists of liver-resident MoMF and blood monocytes trapped in the liver. Very likely due to the rapid and efficient clearance of intrahepatic liposomes by Kupffer cells, other phagocytes in the liver like MoMF only ingested low amounts of the nano- and microcarrier materials. In addition, the mean fluorescence intensity of Kupffer cells after liposome injection was 10-times higher compared to MoMF, suggesting a higher number of carriers per cell due to the higher phagocytic potential of these cells. Liposomes were the only carrier that targeted intrahepatic DC (40% positive after 14 h, Suppl. Fig. 4), which not only control T-cell responses but can also activate hepatic stellate cells in chronic liver disease and thereby promote fibrosis [48].

2.5. Intrahepatic targeting properties of mannosylated polymers

In the liver, polymers were mainly found inside Kupffer cells and endothelial cells. We next evaluated, if modifications of the polymers with targeting ligands, like sugar moieties, changes the cellular biodistribution. Therefore, we employed polymers that were functionalized with mannose to target the mannose receptor (CD206), which is present on macrophages [49]. Mannosylation of various drug carriers was performed in previous studies with the aim of targeting M2 polarized $CD206^{+}$ tumor-associated macrophages [50,51]. In those studies, a preferential uptake by tumor tissue was detectable, but in addition also an increased uptake in the liver was observed. In the liver, CD206 expression is reported for a fraction of Kupffer cells (20% in C57BL6/J mice [52]) as well as liver sinusoidal endothelial cells [53]. Using mannosylated and unmodified pHPMA polymers, we analyzed uptake by myeloid and lymphoid cells in blood, bone marrow, lung, liver and spleen using flow cytometry. In all organs except for the liver, no significant differences in uptake were detected between the two polymers (data not shown). In the liver, there was a markedly enhanced accumulation of mannose-conjugated polymers, which was clearly visible using fluorescence microscopy (Fig. 6A). As expected, mannosylation led to increased carrier uptake by endothelial cells (Fig. 6B) as well as by $CD206^{+}$ Kupffer cells (Fig. 6C). Interestingly, mannosylation of the polymer specifically enhanced the endothelial and $CD206^{+}$ Kupffer cell targeting without affecting uptake by neutrophils, dendritic cells, MoMF or $CD206^{-}$ Kupffer cells (Fig. 6D). Thus, we show that the cell type-specific targeting properties of drug delivery systems can be promoted by including targeting ligands.

2.6. Myeloid subset targeting in spleen, lung and kidney by nano- and microcarriers

To further analyze carrier uptake in other organs, we used standardized methodologies for myeloid cell analysis in peripheral organs such as spleen, lung and kidney. The spleen serves as the major reservoir for circulating leukocytes and is part of the mononuclear phagocyte system. Carrier-positive cells were visible in the red pulp (Suppl. Fig. 2) in direct proximity to the macrophages tagged with latex microspheres, leading to several double-positive cells (Fig. 7A). All three carriers were taken up by a high number of red pulp macrophages ($CD11b^{lo}F4/80^{hi}$, Fig. 7B–C and

Suppl. Fig. 5). These cells have been shown to be efficient in the clearance of intravenously injected carriers [16]. In addition, granulocytes showed a significant polymer uptake (20% carrier positive after 4 h, Fig. 7C–D).

In the lung, there are two major phagocyte populations present, alveolar macrophages (defined as $CD11c^{hi}F4/80^{+}CD11b^{lo}$ cells with a high autofluorescence) and interstitial macrophages (defined as $CD11c^{lo}CD11b^{+}F4/80^{+}$) [54]. Specific gating strategies allowed clear separation of the different myeloid cell populations, including monocytes ($CD11b^{+}F4/80^{-}$) passing the lung (Suppl. Fig. 7).

Ex vivo TPLSM imaging revealed a low density of all different carriers in the lung after intravenous administration, showing only scattered and singular cells being positive for microbubbles, liposomes or polymers (Fig. 8A). Lung-associated monocytes and interstitial macrophages were the major populations taking up microbubbles in the lung (Fig. 8B–C). In contrast to all other cell populations, interstitial macrophages showed an increase in microbubble positive cells between 4 h and 14 h after injection (1.7% compared to 5.8%), (Fig. 8D). In line with other studies [5], microbubbles can indeed be retained intravascularly in the lung; therefore interstitial macrophages might gradually remove microbubbles deposited in the lung. Almost all interstitial macrophages were positive for liposomes, which might explain the high signal seen in FMT 4 h after injection (Fig. 2). In addition, $CD11b^{+}$ DC, which have been described as the antigen-presenting cell in allergic airway disease [55], took up liposomes (around 25%, Suppl. Fig. 8). Polymers showed a broad distribution of carrier-positive cells in the lung, targeting interstitial macrophages, monocytes and alveolar macrophages to a similar degree.

Alveolar macrophages, which are the major phagocyte subset in the lung, stayed negative for the larger particles like microbubbles and liposomes, but showed uptake of polymers. Likely, the anatomical location of the cells inside the alveolar space occludes these cells from the larger circulating carriers. Apparently, only small carrier materials such as 10 nm-sized pHPMA polymers were capable of targeting cells occluded by biological barriers [56]. Uptake of nanocarriers by alveolar macrophages, however, has been linked to inflammatory response of these cells, implying that unintentional targeting of these cells might lead to toxic side effects [57].

There is scarce knowledge on the targeting properties of drug delivery systems to immune cells in the kidney. While no fluorescent signal was visible in the kidney after injection of microbubbles or polymers (Fig. 9A–C), liposomes were visible by *ex vivo* TPLSM in the glomerular compartment and in interstitial cells surrounding the tubular cells (Fig. 9A). These peritubular cells were characterized as kidney dendritic cells using flow cytometry. This showed, that both major kidney myeloid subpopulations (Fig. 9B and Suppl. Fig. 9) were targeted with high efficiency by liposomes that labeled resident DC with an efficacy of almost 80% and monocyte-derived conventional DC with around 60% (Fig. 9C–D). DC are the primary cells responsible for uptake and presentation of proteins reabsorbed from the tubulointerstitial system. These cells lead to immunogenic reactions in the kidney under inflammation that can progress to immune-mediated kidney failure [58,59]. Therefore, targeted drug delivery to these cells might be of interest in tailoring kidney immunity.

It is important to note that lymphocytes only showed a minor uptake of liposomes (less than 6% positive in all lymphocytic cells) and were not targeted by either microbubbles or polymers in various organs (Suppl. Fig. 11).

2.7. Novel clinically relevant target cell populations

By combining whole-body imaging, microscopic imaging and

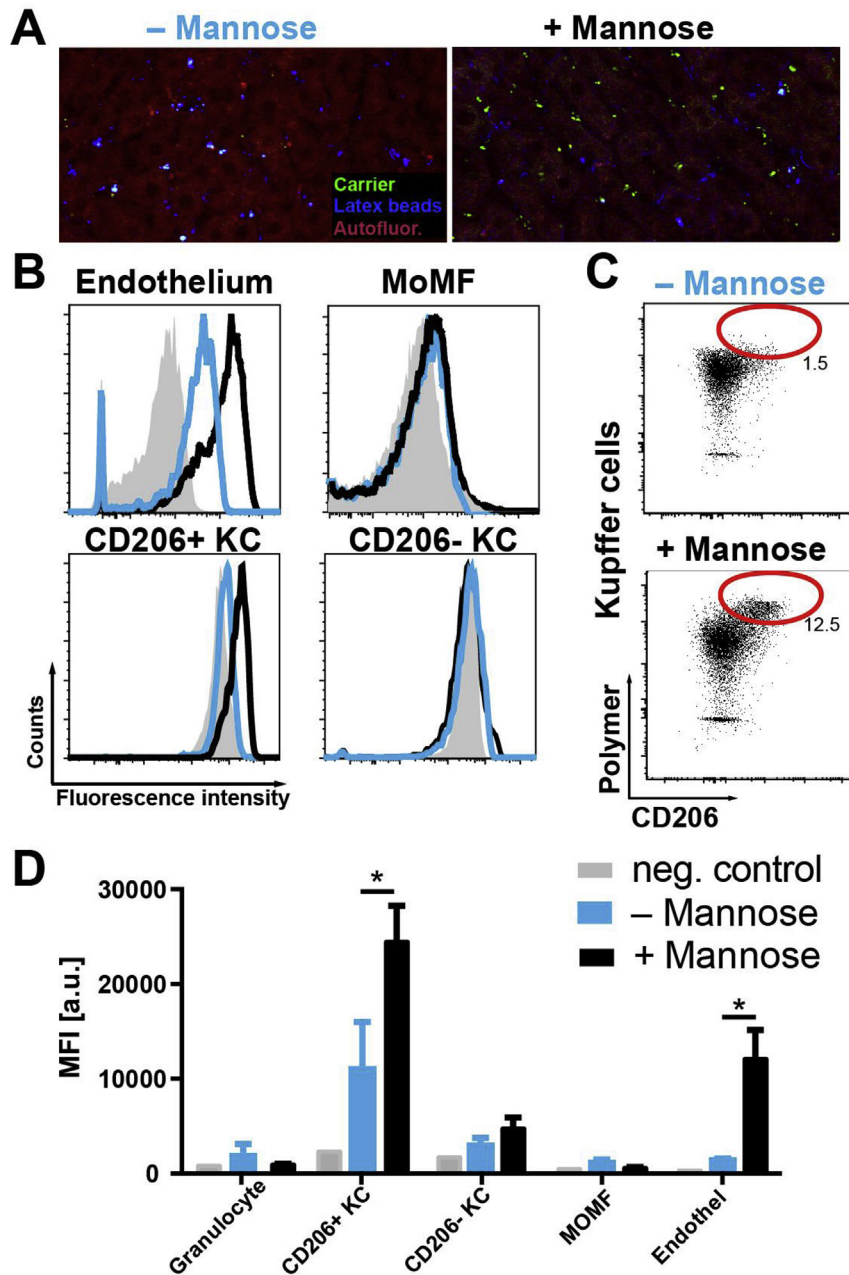


Fig. 6. Active targeting of intrahepatic cells using mannosylated polymers. (A) Fluorescence microscopy images of liver sections from mice 48 h after i.v. injection of pHPMA polymers (green) without (left) and with (right) mannose. Fluorescent latex beads (labeling Kupffer cells) are shown in blue and tissue autofluorescence in red. (B) Endothelial cells were defined as $CD45^- CD31^+$ by flow cytometry, monocyte-derived macrophages (MoMF) as $F4/80^{int} CD11b^+$ and Kupffer cells ($F4/80^+ CD11b^{int}$) were further subdivided based on their expression of CD206. The signal in flow cytometry is shown for plain polymers (blue) and mannose-conjugated polymers (black) as a histogram, the grey signal represents the cell-specific negative control. The axis is logarithmic. There is a marked increase of polymers after conjugation with mannose in CD206⁺ Kupffer cells and in liver endothelial cells. (C) Representative flow cytometry plots show marked increase of in the number of polymer-positive CD206⁺ Kupffer cells with mannosylated carriers. (D) Mean fluorescence intensity (MFI) of the various hepatic cell populations, demonstrating a specific increase of polymer uptake for mannosylated polymers in CD206⁺ Kupffer and endothelial cells. * $P < 0.05$. (For interpretation of the references to colour in this figure legend, the reader is referred to the web version of this article.)

flow cytometry-based cell profiling, we were able to define novel target cell populations and quantify the contribution of various cell types to nano- and microcarrier uptake (Fig. 10, Suppl. Fig. 12). Using *in* and *ex vivo* two-photon microscopy no uptake was visible in parenchymal cells. These previously unrecognized target cell populations might be used for novel treatment approaches in the future. However, further investigations are necessary to develop such organ- and cell type-specific therapies, including the determination of the (altered) cellular biodistribution under disease conditions.

Microbubbles led to a rapid and almost exclusive targeting of mature organ-resident macrophages and Ly-6C^{lo} blood monocytes. This cell population initiates the inflammatory response during distinct types of tissue infection or inflammatory arthritis, and targeting this cell type might be beneficial to prevent excessive tissue damage [60,61]. Since the number of microbubble-positive cells was low (15% positive red pulp macrophages), therapeutic approaches might depend on repetitive carrier application to target a higher ratio of these cells. Microbubbles appear suitable to target Kupffer cells that could ameliorate systemic inflammatory diseases,

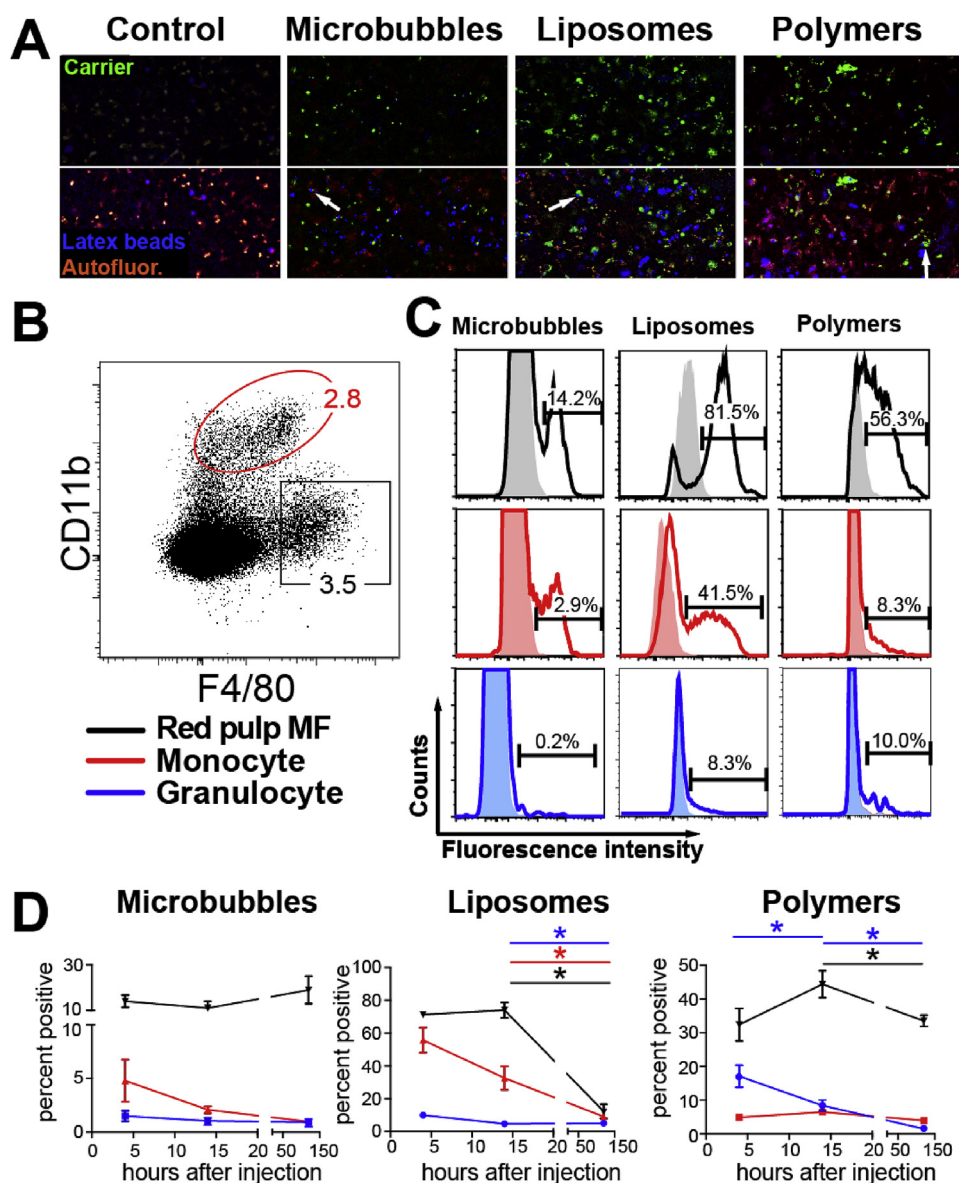


Fig. 7. Nano- and microcarrier accumulation in splenic myeloid immune cells. (A) The top part of the images shows the carrier signal 14 h after injection, the lower part an overlay of fluorescent latex beads (blue) and tissue autofluorescence (orange). Arrows indicate representative cells with colocalization of carriers (in green) with latex microspheres positive professional phagocytes (in blue). (B) Red pulp macrophages were gated as F4/80⁺CD11b^{lo}, and monocytes were defined as CD11b⁺. (C) The signal in flow cytometry is shown as a histogram without (filled areas) and with (14 h after injection, lines) injection of each carrier; histogram gates show the ratio of carrier-positive cells. Red pulp macrophages and monocytes took up all three carriers, while granulocytes only took up polymers and liposomes. Negative histogram peaks are cropped to visualize also low numbers of carrier-positive cells. (D) The carrier distribution (indicated as percent positive cells in the subset) was measured 4, 14 and 120 h after injection; significance is shown for neighboring time points. This shows a stable signal for microbubbles as well as polymers, while the liposome signal decreased over time. **P* < 0.05. (For interpretation of the references to colour in this figure legend, the reader is referred to the web version of this article.)

as shown for protecting mice against autoimmune kidney disease [36]. In addition, interstitial macrophages were targeted by microbubbles, which might have major therapeutic potential because these cells have an immunoregulatory function in diseases like asthma [62] or interstitial lung fibrosis [63].

Interestingly, liposomes were the only carrier type able to target DC. Liver DC can produce significant amounts of tumor necrosis factor and induce activation of hepatic stellate cells in chronic liver disease. Therefore, targeting DC seems an attractive approach for the treatment of liver diseases [48] and may play a yet unrecognized role contributing to the beneficial effect of liposomes for the treatment of experimental liver fibrosis [23]. In the lung, CD11b⁺ DC that have been described as the primary antigen-presenting

cells in allergic airway disease [55] effectively took up liposomes (around 25% positive, Suppl. Fig. 9). Targeted antigen delivery to pulmonary DC might be effective in desensitization approaches [64]. Liposomes even targeted DC in the kidney. While these cells propagate anti-inflammatory immune reactions under homeostasis [65], they also orchestrate immunogenic reactions leading to immune-mediated kidney failure [58,59]. Targeted drug delivery to these cells might therefore be of interest for tailoring kidney immunity and it may reduce the use of systemic immunosuppressants in diseases like ANCA-associated glomerulonephritis [66].

Polymers were the only carrier efficiently labeling endothelial cells in the liver; these cells have a general immunoregulatory phenotype, which potentially ameliorates autoimmune diseases in

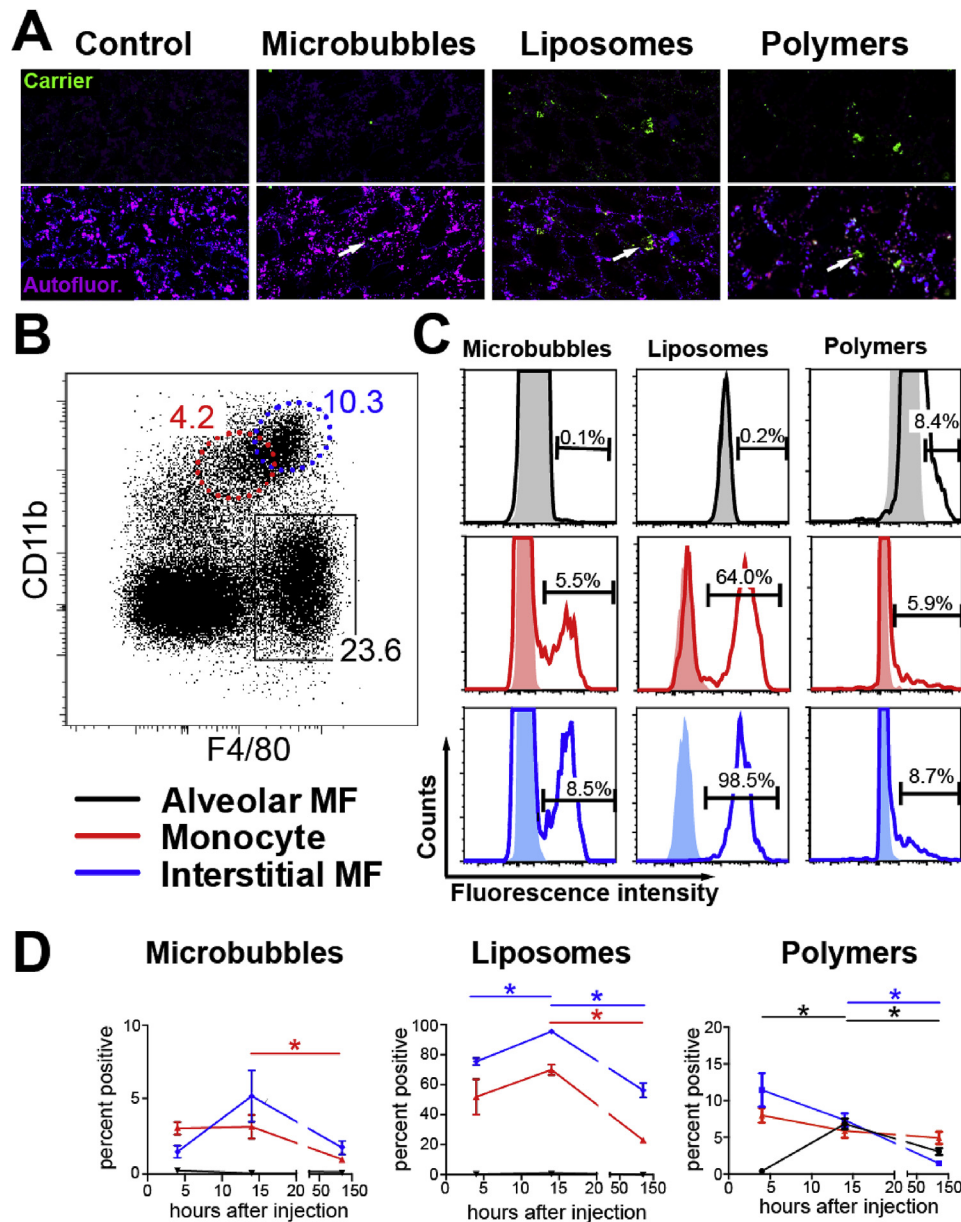


Fig. 8. Nano- and microcarrier accumulation in pulmonary myeloid immune cell populations. (A) The top part of the images shows the carrier signal 14 h after injection only, the lower part an overlay with tissue autofluorescence (purple). Arrows indicate carrier-positive cells (in green). (B) Alveolar macrophages (MF) were gated in flow cytometry as $CD11c^+F4/80^+CD11b^-$ autofluorescent cells. Differentiation of interstitial macrophages and monocytes by F4/80 and CD11b leads only to a rough estimation of the cell subsets (dotted lines), accurate gating that is used for particle uptake quantification is provided in Suppl. Fig. 7 (C) The signal in flow cytometry is shown as a histogram without (filled areas) and with (14 h after injection, lines) injection of each carrier; histogram gates show the ratio of carrier-positive cells. Interstitial macrophages took up all three carriers, while alveolar macrophages only took up polymers. Negative histogram peaks are cropped to also visualize low numbers of carrier-positive cells. (D) The carrier distribution (indicated as percent positive cells in the subset) was measured 4, 14 and 120 h after injection; significance is shown for neighboring time points. This shows a decreasing signal over time for all three carriers. * $P < 0.05$. (For interpretation of the references to colour in this figure legend, the reader is referred to the web version of this article.)

other organs, like experimental autoimmune encephalomyelitis, by delivering nanoparticles to liver endothelium, which induces tolerogenic T-cells [67]. Moreover, polymers were the only carrier materials that were able to efficiently target granulocytes. In the spleen, these cells have been shown to regulate B cell functions and defects in this system lead to systemic infections with mucosal bacteria [68]. Therefore, targeting these cells as an adjuvant against mucosal infections could imply a potential therapeutic application. In other organs, the uptake of polymers by granulocytes can be used in the treatment of inflammatory diseases using the preferential accumulation of neutrophils to inflamed tissue [39] and to modulate their activation in sepsis [69].

3. Conclusions

We here evaluated the myeloid cell targeting ability of three prototypic nano- to micrometer-sized carrier materials that differ in a variety of carrier properties using a multiscale and kinetic approach to study their cellular biodistribution. We show that flow cytometric assessment of carrier distribution in specific cell types and tissues is feasible, and leads to a detailed prediction of target cell populations compared to conventional imaging-based methods. We were able to identify novel target cell populations that bear therapeutic potential for new approaches in targeted therapy. Microbubbles are efficient in rapidly delivering drugs to

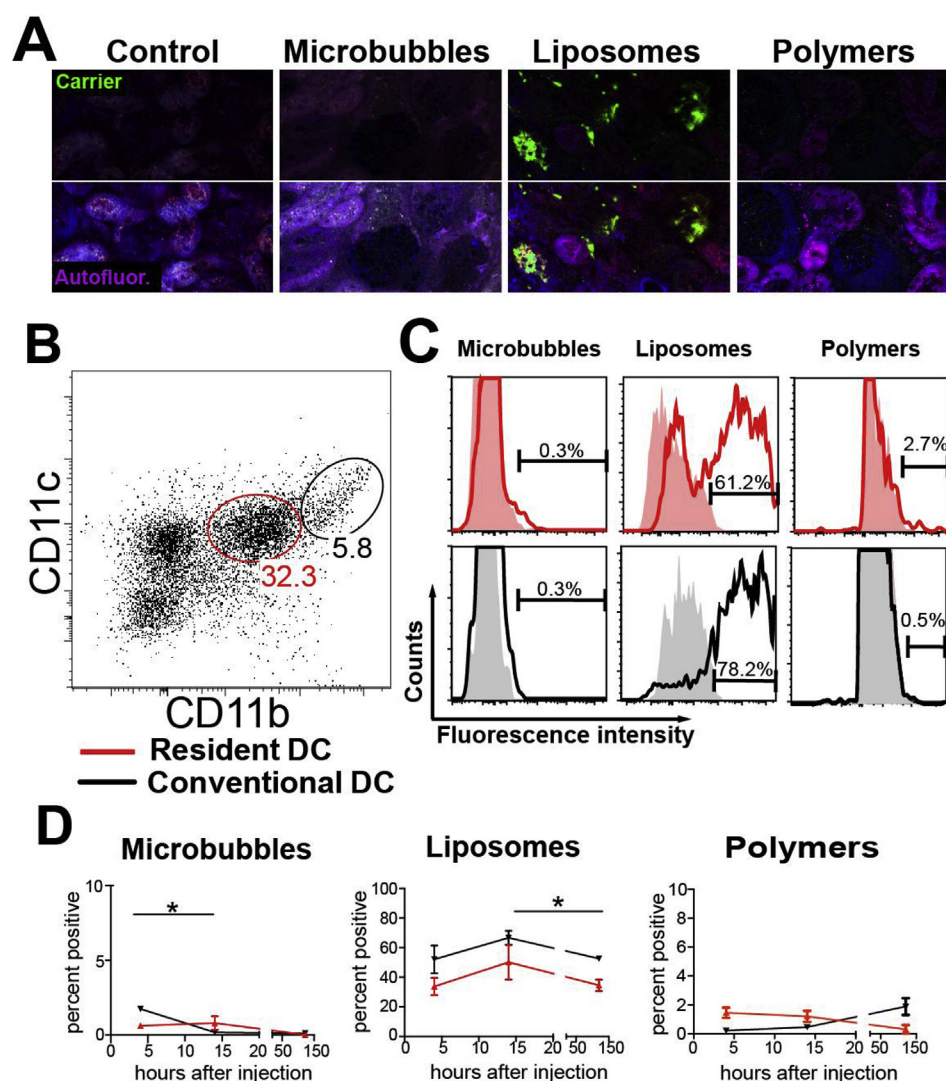


Fig. 9. Nano- and microcarrier accumulation in renal myeloid immune cell populations. (A) The top part of the images shows the carrier signal 14 h after injection, the lower part an overlay with tissue autofluorescence (purple). Glomeruli and peritubular cells were positive after liposome injection. (B) Kidney DC were separated as conventional ($CD11c^+CD11b^{hi}$) and resident DC ($CD11c^+CD11b^{int}$). (C) The signal in flow cytometry is shown as a histogram without (filled areas) and with (14 h after injection, lines) injection of each carrier; histogram gates show the ratio of carrier-positive cells. Only liposomes targeted renal dendritic cells. (D) The carrier distribution (indicated as percent positive cells in the subset) was measured 4, 14 and 120 h after injection; significance is shown for neighboring time points. This shows a constant number of liposome-positive cells over time. * $P < 0.05$. (For interpretation of the references to colour in this figure legend, the reader is referred to the web version of this article.)

professional phagocytes, liposomes are efficient in targeting DC and polymers target endothelial cells of the liver and alveolar macrophages. By mannosylation of polymers, we showed that the cellular biodistribution can be shaped to an increased uptake by liver endothelial cells and mannose receptor-positive Kupffer cells. Further modifications of drug delivery platforms may improve their intrinsic targeting properties and that analyzing the cellular distribution using flow cytometry leads to the identification of the cell type that is responsible for increased organ accumulation.

4. Material and methods

4.1. Synthesis and characterization of carrier materials

Microbubbles with a poly(butyl cyanoacrylate) (PBCA) shell were synthesized as described previously [70]. Briefly, *N*-butyl cyanoacrylate monomer was added drop-wise to a 1% (w/v) TritonX-100 solution at pH 2.5, together with the dye molecules

Rhodamine-B and 1,1,3,3,3-Hexamethylindotricarbocyanine (HITC) iodide. The mixture was stirred at 10,000 rpm for 60 min using an Ultra-turrax (IKA-Werke, Germany), forming dye-loaded microbubbles with a mean diameter of 2 μ m.

Liposomes were synthesized as described in Ref. [23], and were labeled with Alexa Fluor 750 and Alexa Fluor 488 via a post-insertion method. Post-insertion was done using 1,2-distearoyl-*sn*-glycero-3-phosphoethanolamine-*N*-[amino(polyethylene glycol)-2000] (PEG(2000)-DSPE)- and PEG(2000)-DSPE-NH₂-based mixed micelles, to which NHS esters of Alexa Fluor 750 and Alexa Fluor 488 were covalently linked. PEG(2000)-DSPE-NH₂ was present in 5-fold excess compared to both fluorophores. The double labeled micelles were added to the liposomes and the mixture was heated 3 times for 5 min to 60 °C followed by 10 min at room temperature. Upon multiple rounds of extrusion, liposomes with a diameter of 100 nm were obtained.

Polymer synthesis was performed as described in Ref. [20]. In short, random copolymer precursor was synthesized by radical

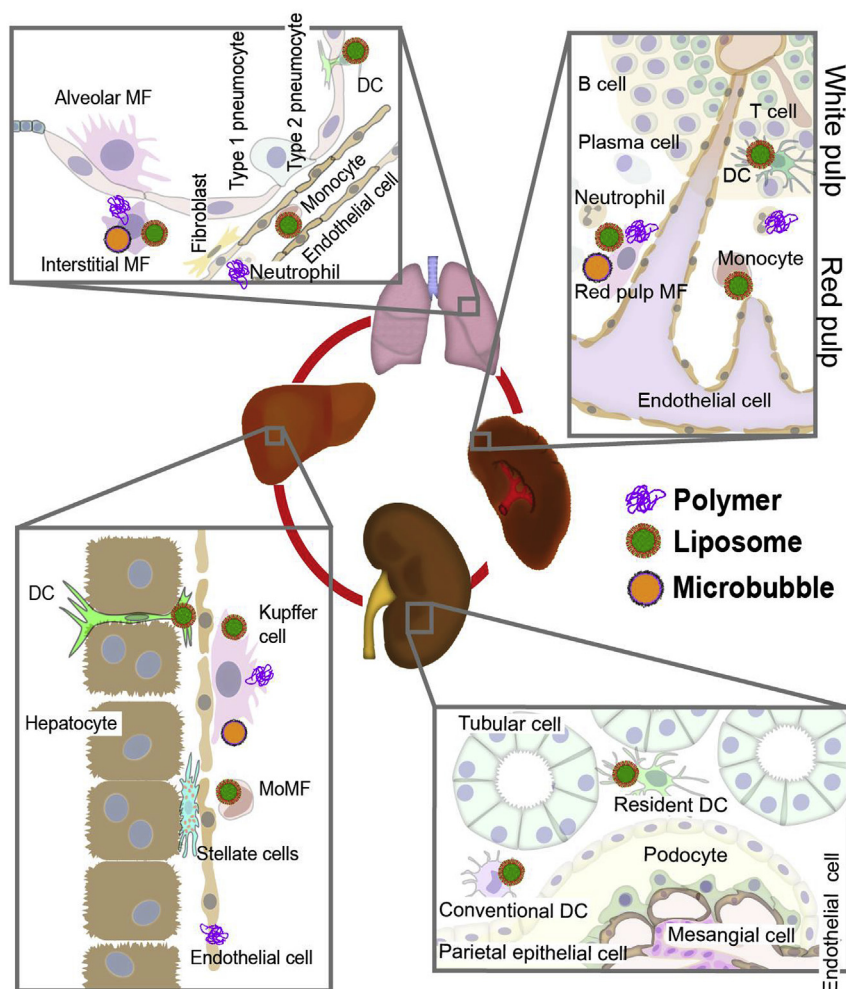


Fig. 10. Schematic nano- and microcarrier accumulation in myeloid cells of different organs. The cellular composition of liver (lower left), lung (top left), spleen (top right) and kidney (lower right) is shown in a schematic way, displaying major findings on myeloid cell targeting by the different carrier materials. In the lung, all carriers were found in interstitial macrophages, while only liposomes were detected in DC and only polymers were detected in alveolar macrophages. In the kidney, only liposomes targeted resident and conventional DC. In the liver, all carriers were found in Kupffer cells, while polymers also efficiently labeled endothelial cells, and liposomes also DC. In the spleen, all carriers were found in red pulp macrophages, while only polymers were found in neutrophils, and only liposomes in DC. These data can serve as a starting point for novel therapeutic approaches targeting distinct myeloid cell subsets in inflammatory diseases. (For interpretation of the references to colour in this figure legend, the reader is referred to the web version of this article.)

copolymerization of (N-2-hydroxypropyl)methacrylamide (HPMA, 85 mol %) and 3-(N-methacryloylglycylglycyl) thiazolidine-2-thione (Ma-GG-TT, 15 mol %) in dimethyl sulfoxide (DMSO) at 50 °C for 6 h. Poly(HPMA-co-Ma-GG-TT) was dissolved in methanol and N,N-Diisopropylethylamine, together with the fluorophores ATTO 488-NH₂ and Dy750-NH₂. After 30 min reaction, the polymer was aminolyzed with 1-aminopropan-2-ol, followed by precipitation using diethylether and centrifugation. Purification was performed by gel filtration on Sephadex G-25 in water (PD 10 column; Pharmacia). The molecular weight of the polymer was 67 kDa, its polydispersity index was 1.7, and the content of both dyes was 2.5 wt%.

The synthesis of mannose containing poly-HPMA polymers was performed as described [71] and by applying the polymer synthesis and postpolymerization modification conditions of [72]. As an example, 70.0 mg of the reactive ester precursor polymer poly(-PFMA) P1 and 2.76 μmol (0.01 eq.) of the fluorescent dyes Oregon Green 488 cadaverine and Cy7.5 cadaverine were dissolved in 1.5 ml dioxane and 1.5 ml DMF. This solution was stirred at 50 °C overnight. Afterwards, 9.9 mg (27.8 μmol, 0.05 eq. regarding to the reactive ester groups) mannose and NET3 as a base were added and

stirred for 24 h. Incorporated mannose was quantified by inverse gated ¹³C NMR spectroscopy. The final mannose content was determined to be 3 wt%. Thereafter, 84.0 μl (83.0 mg, 1.11 mmol, 4.0 eq.) of 2-hydroxyaminopropanol and 192 μl (140 mg, 1.38 mmol, 5.0 eq. regarding to the reactive ester groups) of triethylamine were added and the reaction was stirred for 3 days at 50 °C under argon atmosphere. Finally, for purification, the polymer solution was diluted with Milli-Q water and dialyzed for 3 days using Spectra/Por membranes (MW cut-off 3500 g/mol).

4.2. Mice

C57BL6/J and hairless SKH1-e mice were kept under specific pathogen-free environmental conditions. All experiments were performed with mixed gender mice at 9–14 weeks of age under ethical conditions approved by the appropriate authorities according to German legal requirements. All carriers have already been used for in vivo application at similar doses, where toxicity was excluded using standard assays [20,23,73]. SKH1-e mice were used for FMT-CT experiments, since these mice exhibit a functioning thymus gland but are hairless and therefore better suited

for optical imaging. C57BL6/J mice were used for flow cytometry and microscopy because the used antibodies are validated to bind to epitopes in these mice. Control and experimental group were housed in the same cage and were allocated at the time point of injection.

4.3. Flow cytometric analysis

Mice were injected with the respective carrier 4, 14 and 120 h before analysis. Carriers were diluted in 200 μ l of NaCl and injected at a dose of 10^7 microbubbles, and 2 nmol of fluorophore for liposomes and polymers. Data concerning the cellular biodistribution of mannosylated polymers was assessed 48 h after injection. Flow cytometric analysis of tissue leukocytes was performed as described earlier [74]. In brief, the various tissues were digested with collagenase type-IV (Worthington) at 37 °C with collagenase solution. Extracts were filtered using 70 μ m cell strainers (BD Bioscience), and parenchymal cells were removed by sedimentation for 45 min at 4 °C followed by centrifugation for 5 min at 15 g. Blood was obtained by cardiac puncture. Tissue lysates were subjected to erythrocyte lysis buffer by Pharmlyse (BD Bioscience), washed with PBS and stained with fluorochrome-conjugated antibodies in Hank's balanced salt solution (HBSS) containing 0.1 mM EDTA, 2% bovine serum albumin (BSA) and unconjugated anti-CD16/32 (Fc block, BD). After 30 min unbound antibody was washed with HBSS, and 7-AAD was added for life/dead discrimination staining. Staining was performed using combinations of the following monoclonal antibodies: Gr-1, CD11b, CD4, CD45, Ly-6G, CD31, NK1.1, CD11c, CD206 (BD Bioscience), CD8a, F4/80 (Biolegends), I-A^b, CD3, CD19 (eBioscience). Flow cytometric analysis was performed using a FACS Fortessa (BD). Data were analyzed using FlowJo (TreeStar). Flow cytometric data are given as percentages of total leukocytes; the number of carrier-positive cells is given as percentage of the respective cell type. Microbubbles were excited by a 561 nm yellow-green laser and recorded with a 582/15 nm filter, polymers and liposomes were excited by a 488 nm blue laser and recorded with a 530/30 nm filter. There was a clear segregation between carrier-positive and negative cells in all groups. The PMT voltage in the liposome group was reduced compared to the polymer group to avoid overexposition.

4.4. Ex vivo histological analysis

Carriers were diluted in 200 μ l of NaCl and injected 14 h before analysis at a dose of 10^7 microbubbles, and 2 nmol of fluorophore for liposomes and polymers. Cryosections were prepared for epifluorescence microscopy with a thickness of 5 μ m and analyzed using a Zeiss Axio Observer fluorescence microscope (Carl Zeiss). For ex vivo two-photon microscopy, mice were perfused by intracardiac injection of 4 ml of formaline 4% (v/v) directly after euthanasia and incision into the right femoral artery followed by 4 ml of HBSS to reduce autofluorescence by necrotic cells. Kidneys were halved to expose glomeruli. The other organs were left as excised and imaged using an Olympus Fluoview FV1000 MPE two-photon microscope.

4.5. Intravital two-photon laser scanning microscopy (TPLSM)

Anesthesia was performed using ketamine/xylazine (100 and 10 mg/kg, intraperitoneally), followed by surgical tracheotomy and controlled respiration with 2.5% isoflurane in pure oxygen. Intravital TPLSM was performed as described earlier [34]. Kupffer cells were labeled by intravenous injection of 1 μ m blue fluorescent latex microspheres (Life Technologies, Carlsbad) with a concentration of 0.04% (v/v) 2 h previous to TPLSM. Fluorescent carriers were

injected into the right ventricle at a dose of 5×10^7 microbubbles, and 2 nmol of fluorophore with liposomes and polymers after the first minutes of imaging and their distribution was monitored over at least 2 h. Video sequence analysis was performed using IMARIS (7.7.2; Bitplane AG, Zürich, Switzerland) and Ilastik software (version 1.1.2) [75]. The quantification of both segmented regions (vasculature and Kupffer cells) was performed on background-subtracted images.

4.6. Fluorescence-mediated tomography (FMT) and micro-computed tomography (μ CT)

Constructs were injected intravenously via a tail vein catheter (respective 2 nmol fluorophore, approximately 2×10^7 microbubble, diluted in 0.9% NaCl, 100 μ l injection volume). Optical whole-body imaging was performed before injection of the carriers as well as 15 min, 4, 8, 24, 48 and 120 h after carrier injection using an FMT-scanner measuring fluorescence emission (FMT2500 LX, PerkinElmer). Mice were anesthetized using isoflurane (2% v/v) during the time of imaging and were kept in a fixed position for the μ CT and FMT scans [29]. For anatomical localization and attenuation correction, a μ CT scan was performed directly before the FMT measurement using a μ CT system (Tomoscopes Duo, CT-Imaging GmbH, Germany) as described earlier [28]. Fluorescence was quantified using the Imalytics Preclinical software [76]. The total fluorescence intensity was evaluated by normalization to the total fluorescence intensity in the whole mouse 15 min after injection.

5. Statistical analysis

Statistical data analysis was performed using PRISM software (Version 6, GraphPad Software Inc., La Jolla, CA), and data are expressed as mean \pm standard error of the mean. Differences between groups were assessed by means of a two-tailed unpaired Student *t*-test. P-values were corrected according to Bonferroni-correction, when multiple tests were performed.

Acknowledgements

We thank Dr. Stanley Fokong for assistance with microbubble synthesis and characterization. This work was supported by the German Research Foundation (DFG; Ta434/3-1, SFB/TRR57, La2937/1-2, SFB1066), the Interdisciplinary Center for Clinical Research (IZKF) (E7-1 and O2-3) Aachen, the European Research Council (ERC; StG-309495), the German Cancer Foundation (70112418) (Mildred-Scheel-Doktorandenprogramm) and the German Ministry for Education and Research (BMBF, BioPhotonics) (13N13355) with co-funding from the European Union Seventh Framework Programme.

Appendix A. Supplementary data

Supplementary data related to this article can be found at <http://dx.doi.org/10.1016/j.biomaterials.2016.11.009>.

References

- [1] D. Peer, J.M. Karp, S. Hong, O.C. Farokhzad, R. Margalit, R. Langer, Nanocarriers as an emerging platform for cancer therapy, *Nat. Nanotechnol.* 2 (12) (2007) 751–760.
- [2] O.C. Farokhzad, R. Langer, Impact of nanotechnology on drug delivery, *ACS Nano* 3 (1) (2009) 16–20.
- [3] M.E. Davis, Z.G. Chen, D.M. Shin, Nanoparticle therapeutics: an emerging treatment modality for cancer, *Nat. Rev. Drug Discov.* 7 (9) (2008) 771–782.
- [4] X. Huang, F. Zhang, L. Zhu, K.Y. Choi, N. Guo, J. Guo, K. Tackett, P. Anilkumar, G. Liu, Q. Quan, H.S. Choi, G. Niu, Y.P. Sun, S. Lee, X. Chen, Effect of injection routes on the biodistribution, clearance, and tumor uptake of carbon dots, *ACS*

- Nano 7 (7) (2013) 5684–5693.
- [5] A. Barrefelt, Y. Zhao, M.K. Larsson, G. Egri, R.V. Kuiper, J. Hamm, M. Saghaian, K. Caidahl, T.B. Brismar, P. Aspelin, R. Heuchel, M. Muhammed, L. Dahne, M. Hassan, Fluorescence labeled microbubbles for multimodal imaging, *Biochem. Biophys. Res. Commun.* 464 (3) (2015) 737–742.
 - [6] S. Kunjachan, J. Ehling, G. Storm, F. Kiessling, T. Lammers, Noninvasive imaging of nanomedicines and nanotheranostics: principles, progress, and prospects, *Chem. Rev.* 115 (19) (2015) 10907–10937.
 - [7] Y. Shi, R. van der Meel, B. Theek, E. Oude Blenke, E.H. Pieters, M.H. Fens, J. Ehling, R.M. Schiffelers, G. Storm, C.F. van Nostrum, T. Lammers, W.E. Hennink, Complete regression of Xenograft tumors upon targeted delivery of paclitaxel via pi-pi stacking stabilized polymeric micelles, *ACS Nano* 9 (4) (2015) 3740–3752.
 - [8] B. Silva-Santos, K. Serre, H. Norell, $\gamma\delta$ T cells in cancer, *Nat. Rev. Immunol.* 15 (11) (2015) 683–691.
 - [9] D.I. Gabrilovich, S. Nagaraj, Myeloid-derived suppressor cells as regulators of the immune system, *Nat. Rev. Immunol.* 9 (3) (2009) 162–174.
 - [10] F. Heymann, F. Tacke, Immunology in the liver—from homeostasis to disease, *Nat. Rev. Gastroenterol. Hepatol.* 13 (2) (2016) 88–110.
 - [11] S.-D. Li, L. Huang, Pharmacokinetics and biodistribution of nanoparticles, *Mol. Pharm.* 5 (4) (2008) 496–504.
 - [12] H. Soo Choi, W. Liu, P. Misra, E. Tanaka, J.P. Zimmer, B. Itty Ipe, M.G. Bawendi, J.V. Frangioni, Renal clearance of quantum dots, *Nat. Biotechnol.* 25 (10) (2007) 1165–1170.
 - [13] R. Weissleder, M. Nahrendorf, M.J. Pittet, Imaging macrophages with nanoparticles, *Nat. Mater.* 13 (2) (2014) 125–138.
 - [14] F. Alexis, E. Pridgen, L.K. Molnar, O.C. Farokhzad, Factors affecting the clearance and biodistribution of polymeric nanoparticles, *Mol. Pharm.* 5 (4) (2008) 505–515.
 - [15] E. Blanco, H. Shen, M. Ferrari, Principles of nanoparticle design for overcoming biological barriers to drug delivery, *Nat. Biotechnol.* 33 (9) (2015) 941–951.
 - [16] A.E. Nel, L. Madler, D. Velegol, T. Xia, E.M.V. Hoek, P. Somasundaran, F. Klaessig, V. Castranova, M. Thompson, Understanding biophysics/chemical interactions at the nano-bio interface, *Nat. Mater.* 8 (7) (2009) 543–557.
 - [17] E.J. Keliher, J. Yoo, M. Nahrendorf, J. Lewis, B. Marinelli, A. Newton, M. Pittet, R. Weissleder, (89)Zr labeled Dextran nanoparticles enable in vivo macrophage imaging, *Bioconjugate Chem.* 22 (12) (2011) 2383–2389.
 - [18] Y.W. Yang, W.H. Luo, Cellular biodistribution of polymeric nanoparticles in the immune system, *J. Control. Release* 227 (2016) 82–93.
 - [19] S. Kunjachan, R. Pola, F. Gremse, B. Theek, J. Ehling, D. Moeckel, B. Hermanns-Sachweh, M. Pechar, K. Ulbrich, W.E. Hennink, G. Storm, W. Lederle, F. Kiessling, T. Lammers, Passive versus active tumor targeting using RGD- and NGR-modified polymeric nanomedicines, *Nano Lett.* 14 (2) (2014) 972–981.
 - [20] S. Kunjachan, F. Gremse, B. Theek, P. Koczera, R. Pola, M. Pechar, T. Etrych, K. Ulbrich, G. Storm, F. Kiessling, T. Lammers, Noninvasive optical imaging of nanomedicine biodistribution, *ACS Nano* 7 (1) (2013) 252–262.
 - [21] R. Duncan, M.J. Vicent, Do HPMA copolymer conjugates have a future as clinically useful nanomedicines? A critical overview of current status and future opportunities, *Adv. drug Deliv. Rev.* 62 (2) (2010) 272–282.
 - [22] V.P. Torchilin, Recent advances with liposomes as pharmaceutical carriers, *Nat. Rev. Drug Discov.* 4 (2) (2005) 145–160.
 - [23] M. Bartneck, K.M. Scheyda, K.T. Warzecha, L.Y. Rizzo, K. Hittatiya, T. Luedde, G. Storm, C. Trautwein, T. Lammers, F. Tacke, Fluorescent cell-traceable dexamethasone-loaded liposomes for the treatment of inflammatory liver diseases, *Biomaterials* 37 (2015) 367–382.
 - [24] B.A. Kaufmann, J.M. Sanders, C. Davis, A. Xie, P. Aldred, I.J. Sarembock, J.R. Lindner, Molecular imaging of inflammation in atherosclerosis with targeted ultrasound detection of vascular cell adhesion molecule-1, *Circulation* 116 (3) (2007) 276–284.
 - [25] K. Ferrara, R. Pollard, M. Borden, Ultrasound microbubble contrast agents: fundamentals and application to gene and drug delivery, *Annu. Rev. Biomed. Eng.* 9 (1) (2007) 415–447.
 - [26] S.H. Cheng, F.C. Li, J.S. Souris, C.S. Yang, F.G. Tseng, H.S. Lee, C.T. Chen, C.Y. Dong, L.W. Lo, Visualizing dynamics of sub-hepatic distribution of nanoparticles using intravital multiphoton fluorescence microscopy, *ACS Nano* 6 (5) (2012) 4122–4131.
 - [27] A.L. van de Ven, P. Kim, M. Ferrari, S.H. Yun, Real-time intravital microscopy of individual nanoparticle dynamics in liver and tumors of live mice, *Protoc. Exch.* 2013 (2013), <http://dx.doi.org/10.1038/protex.2013.049>.
 - [28] F. Gremse, B. Theek, S. Kunjachan, W. Lederle, A. Pardo, S. Barth, T. Lammers, U. Naumann, F. Kiessling, Absorption reconstruction improves biodistribution assessment of fluorescent nanoprobes using hybrid fluorescence-mediated tomography, *Theranostics* 4 (10) (2014) 960–971.
 - [29] F. Gremse, D. Doleschel, S. Zafarnia, A. Babler, W. Jahnen-Dechent, T. Lammers, W. Lederle, F. Kiessling, Hybrid μ CT-FMT imaging and image analysis, *J. Vis. Exp.* 100 (2015) e52770.
 - [30] M.A. Markus, J. Napp, T. Behnke, M. Mitkovski, S. Monecke, C. Dullin, S. Kilfeather, R. Dressel, U. Resch-Genger, F. Alves, Tracking of inhaled near-infrared fluorescent nanoparticles in lungs of SKH-1 mice with allergic airway inflammation, *ACS Nano* 9 (12) (2015) 11642–11657.
 - [31] O. Boerman, W. Oyen, G. Storm, M. Corvo, L. van Bloois, J.W.M. van der Meer, F. Corstens, Technetium-99m labelled liposomes to image experimental arthritis, *Ann. Rheum. Dis.* 56 (6) (1997) 369–373.
 - [32] L.W. Seymour, R. Duncan, J. Strohal, J. Kopeček, Effect of molecular weight (Mw) of N-(2-hydroxypropyl)methacrylamide copolymers on body distribution and rate of excretion after subcutaneous, intraperitoneal, and intravenous administration to rats, *J. Biomed. Mater. Res.* 21 (11) (1987) 1341–1358.
 - [33] T. van der Geest, P. Laverman, D. Gerrits, G.M. Franssen, J.M. Metselaar, G. Storm, O.C. Boerman, Comparison of three remote radiolabelling methods for long-circulating liposomes, *J. Control. Release* 220 (Pt A) (2015) 239–244.
 - [34] F. Heymann, P.M. Niemietz, J. Peusquens, C. Ergen, M. Kohlhepp, J.C. Mossanen, C. Schneider, M. Vogt, R.H. Tolba, C. Trautwein, C. Martin, F. Tacke, Long term intravital multiphoton microscopy imaging of immune cells in healthy and diseased liver using CXCR6.Gfp reporter mice, *J. Vis. Exp.* 97 (2015).
 - [35] Y.N. Zhang, W. Poon, A.J. Tavares, I.D. McGilvray, W.C. Chan, Nanoparticle-liver interactions: cellular uptake and hepatobiliary elimination, *J. Control. Release* 240 (2016) 332–348.
 - [36] F. Heymann, J. Peusquens, I. Ludwig-Portugall, M. Kohlhepp, C. Ergen, P. Niemietz, C. Martin, N. van Rooijen, J.C. Ochando, G.J. Randolph, T. Luedde, F. Ginhoux, C. Kurts, C. Trautwein, F. Tacke, Liver inflammation abrogates immunological tolerance induced by Kupffer cells, *Hepatology* 62 (1) (2015) 279–291.
 - [37] W.Y. Lee, T.J. Moriarty, C.H. Wong, H. Zhou, R.M. Strieter, N. van Rooijen, G. Chaconas, P. Kubes, An intravascular immune response to Borrelia burgdorferi involves Kupffer cells and iNKT cells, *Nat. Immunol.* 11 (4) (2010) 295–302.
 - [38] B.R. Smith, E.E. Ghosn, H. Rallapalli, J.A. Prescher, T. Larson, L.A. Herzenberg, S.S. Gambhir, Selective uptake of single-walled carbon nanotubes by circulating monocytes for enhanced tumour delivery, *Nat. Nanotechnol.* 9 (6) (2014) 481–487.
 - [39] D. Chu, J. Gao, Z. Wang, Neutrophil-mediated delivery of therapeutic nanoparticles across blood vessel barrier for treatment of inflammation and infection, *ACS Nano* 9 (12) (2015) 11800–11811.
 - [40] S. Yona, K.-W. Kim, Y. Wolf, A. Mildner, D. Varol, M. Breker, D. Strauss-Ayali, S. Viukov, M. Guillemin, A. Misharin, D.A. Hume, H. Perlman, B. Malissen, E. Zelzer, S. Jung, Fate mapping reveals origins and dynamics of monocytes and tissue macrophages under homeostasis, *Immunity* 38 (1) (2013) 79–91.
 - [41] F. Tacke, F. Ginhoux, C. Jakubzik, N. van Rooijen, M. Merad, G.J. Randolph, Immature monocytes acquire antigens from other cells in the bone marrow and present them to T cells after maturing in the periphery, *J. Exp. Med.* 203 (3) (2006) 583–597.
 - [42] C. Shi, E.G. Pamer, Monocyte recruitment during infection and inflammation, *Nat. Rev. Immunol.* 11 (11) (2011) 762–774.
 - [43] J.M. Metselaar, M.H. Wauben, J.P. Wagenaar-Hilbers, O.C. Boerman, G. Storm, Complete remission of experimental arthritis by joint targeting of glucocorticoids with long-circulating liposomes, *Arthritis Rheum.* 48 (7) (2003) 2059–2066.
 - [44] T. Daemen, M. Velinova, J. Regts, M. de Jager, R. Kalicharan, J. Donga, J.J. van der Want, G.L. Scherphof, Different intrahepatic distribution of phosphatidylglycerol and phosphatidylserine liposomes in the rat, *Hepatology* 26 (2) (1997) 416–423.
 - [45] A. Akhter, Y. Hayashi, Y. Sakurai, N. Ohga, K. Hida, H. Harashima, A liposomal delivery system that targets liver endothelial cells based on a new peptide motif present in the ApoB-100 sequence, *Int. J. Pharm.* 456 (1) (2013) 195–201.
 - [46] A. Schurich, J.P. Bottcher, S. Burgdorf, P. Penzler, S. Hegenbarth, M. Kern, A. Dolf, E. Endl, J. Schultze, E. Wiertz, D. Stabenow, C. Kurts, P. Knolle, Distinct kinetics and dynamics of cross-presentation in liver sinusoidal endothelial cells compared to dendritic cells, *Hepatology* 50 (3) (2009) 909–919.
 - [47] P.A. Knolle, D. Wöhlleber, Immunological functions of liver sinusoidal endothelial cells, *Cell. Mol. Immunol.* 13 (3) (2016) 347–353.
 - [48] M.K. Connolly, A.S. Bedrosian, J. Mallen-St Clair, A.P. Mitchell, J. Ibrahim, A. Stroud, H.L. Pachter, D. Bar-Sagi, A.B. Frey, G. Miller, In liver fibrosis, dendritic cells govern hepatic inflammation in mice via TNF- α , *The Journal of Clin. Invest.* 119 (11) (2009) 3213–3225.
 - [49] A. Mantovani, S. Sozzani, M. Locati, P. Allavena, A. Sica, Macrophage polarization: tumor-associated macrophages as a paradigm for polarized M2 mononuclear phagocytes, *Trends Immunol.* 23 (11) (2002) 549–555.
 - [50] K. Movahedi, S. Schoonooghe, D. Laoui, I. Houbrecken, W. Waelput, K. Breckpot, L. Bouwens, T. Lahoutte, P. De Baetselier, G. Raes, N. Devoogdt, J.A. Van Ginderachter, Nanobody-based targeting of the macrophage mannose receptor for effective in vivo imaging of tumor-associated macrophages, *Cancer Res.* 72 (16) (2012) 4165–4177.
 - [51] L.W. Locke, M.W. Mayo, A.D. Yoo, M.B. Williams, S.S. Berr, PET imaging of tumor associated macrophages using mannose coated 64Cu liposomes, *Biomaterials* 33 (31) (2012) 7785–7793.
 - [52] J. Wan, M. Benkdane, F. Teixeira-Clerc, S. Bonnafous, A. Louvet, F. Lafdil, F. Pecker, A. Tran, P. Gual, A. Mallat, S. Lotersztajn, C. Pavoine, M2 Kupffer cells promote M1 Kupffer cell apoptosis: a protective mechanism against alcoholic and nonalcoholic fatty liver disease, *Hepatology* 59 (1) (2014) 130–142.
 - [53] K. Elvevold, J. Simon-Santamaria, H. Hasvold, P. McCourt, B. Smedsrød, K.K. Sørensen, Liver sinusoidal endothelial cells depend on mannose receptor-mediated recruitment of lysosomal enzymes for normal degradation capacity, *Hepatology* 48 (6) (2008) 2007–2015.
 - [54] R. Zaynagetdinov, T.P. Sherrill, P.L. Kendall, B.H. Segal, K.P. Weller, R.M. Tighe, T.S. Blackwell, Identification of myeloid cell subsets in murine lungs using flow cytometry, *Am. J. Respir. Cell Mol. Biol.* 49 (2) (2013) 180–189.
 - [55] Q. Zhou, A.W. Ho, A. Schlitzer, Y. Tang, K.H. Wong, F.H. Wong, Y.L. Chua,

- V. Angeli, A. Mortellaro, F. Ginhoux, D.M. Kemeny, GM-CSF-licensed CD11b+ lung dendritic cells orchestrate Th2 immunity to *Blomia tropicalis*, *J. Immunol.* Baltim. Md. 1950) 193 (2) (2014) 496–509.
- [56] M. Hemmelmann, V.V. Metz, K. Koynov, K. Blank, R. Postina, R. Zentel, Amphiphilic HPMA-LMA copolymers increase the transport of Rhodamine 123 across a BBB model without harming its barrier integrity, *J. Control. Release* 163 (2) (2012) 170–177.
- [57] R. Liu, X. Zhang, Y. Pu, L. Yin, Y. Li, X. Zhang, G. Liang, X. Li, J. Zhang, Small-sized titanium dioxide nanoparticles mediate immune toxicity in rat pulmonary alveolar macrophages in vivo, *J. Nanosci. Nanotechnol.* 10 (8) (2010) 5161–5169.
- [58] K. Hochheiser, A. Tittel, C. Kurts, Kidney dendritic cells in acute and chronic renal disease, *Int. J. Exp. Pathol.* 92 (3) (2011) 193–201.
- [59] N.M. Rogers, D.A. Ferenbach, J.S. Isenberg, A.W. Thomson, J. Hughes, Dendritic cells and macrophages in the kidney: a spectrum of good and evil, *Nat. Rev. Nephrol.* 10 (11) (2014) 625–643.
- [60] C. Auffray, D. Fogg, M. Garfa, G. Elain, O. Join-Lambert, S. Kayal, S. Sarnacki, A. Cumano, G. Lauvau, F. Geissmann, Monitoring of blood vessels and tissues by a population of monocytes with patrolling behavior, *Science* 317 (5838) (2007) 666.
- [61] A.V. Misharin, C.M. Cuda, R. Saber, J.D. Turner, A.K. Gierut, G.K. Haines, S. Berdnikovs, A. Filer, A.R. Clark, C.D. Buckley, G.M. Mutlu, G.R.S. Budinger, H. Perlman, Non-classical Ly6C(–) monocytes drive the development of inflammatory arthritis in mice, *Cell Rep.* 9 (2) (2014) 591–604.
- [62] D. Bedoret, H. Wallemacq, T. Marichal, C. Desmet, F. Quesada Calvo, E. Henry, R. Closset, B. Dewals, C. Thielen, P. Gustin, L. de Leval, N. Van Rooijen, A. Le Moine, A. Vanderplasschen, D. Cataldo, P.-V. Drion, M. Moser, P. Lekeux, F. Bureau, Lung interstitial macrophages alter dendritic cell functions to prevent airway allergy in mice, *J. Clin. Invest.* 119 (12) (2009) 3723–3738.
- [63] J.M. Vignaud, M. Allam, N. Martinet, M. Pech, F. Plenat, Y. Martinet, Presence of platelet-derived growth factor in normal and fibrotic lung is specifically associated with interstitial macrophages, while both interstitial macrophages and alveolar epithelial cells express the c-sis proto-oncogene, *Am. J. Respir. Cell Mol. Biol.* 5 (6) (1991) 531–538.
- [64] K. Ichikawa, T. Urakami, S. Yonezawa, H. Miyauchi, K. Shimizu, T. Asai, N. Oku, Enhanced desensitization efficacy by liposomal conjugation of a specific antigen, *Int. J. Pharm.* 336 (2) (2007) 391–395.
- [65] F. Heymann, C. Meyer-Schwesinger, E.E. Hamilton-Williams, L. Hammerich, U. Panzer, S. Kaden, S.E. Quaggin, J. Floege, H.J. Grone, C. Kurts, Kidney dendritic cell activation is required for progression of renal disease in a mouse model of glomerular injury, *J. Clin. Invest.* 119 (5) (2009) 1286–1297.
- [66] A. Pani, Standard immunosuppressive therapy of immune-mediated glomerular diseases, *Autoimmun. Rev.* 12 (8) (2013) 848–853.
- [67] A. Carambia, B. Freund, D. Schwinge, O.T. Bruns, S.C. Salmen, H. Ittrich, R. Reimer, M. Heine, S. Huber, C. Waurisch, A. Eychmuller, D.C. Wraith, T. Korn, P. Nielsen, H. Weller, C. Schramm, S. Luth, A.W. Lohse, J. Heeren, J. Herkel, Nanoparticle-based autoantigen delivery to Treg-inducing liver sinusoidal endothelial cells enables control of autoimmunity in mice, *J. Hepatol.* 62 (6) (2015) 1349–1356.
- [68] I. Puga, M. Cols, C.M. Barra, B. He, L. Cassis, M. Gentile, L. Comerma, A. Chorny, M. Shan, W. Xu, G. Magri, D.M. Knowles, W. Tam, A. Chiu, J.B. Bussell, S. Serrano, J.A. Lorente, B. Bellosillo, J. Lloreta, N. Juanpere, F. Alameda, T. Baro, C.D. de Heredia, N. Toran, A. Catala, M. Torreadell, C. Fortuny, V. Cusi, C. Carreras, G.A. Diaz, J.M. Blander, C.-M. Farber, G. Silvestri, C. Cunningham-Rundles, M. Calvillo, C. Dufour, L.D. Notarangelo, V. Lougaris, A. Plebani, J.-L. Casanova, S.C. Ganai, A. Diefenbach, J.I. Arostegui, M. Juan, J. Yague, N. Mahlaoui, J. Donadieu, K. Chen, A. Cerutti, B cell-helper neutrophils stimulate the diversification and production of immunoglobulin in the marginal zone of the spleen, *Nat. Immunol.* 13 (2) (2012) 170–180.
- [69] F. Sonego, J.C. Alves-Filho, F.Q. Cunha, Targeting neutrophils in sepsis, *Expert Rev. Clin. Immunol.* 10 (8) (2014) 1019–1028.
- [70] S. Fokong, M. Siepmann, Z. Liu, G. Schmitz, F. Kiessling, J. Gatzens, Advanced characterization and refinement of poly N-butyl cyanoacrylate microbubbles for ultrasound imaging, *Ultrasound Med. Biol.* 37 (10) (2011) 1622–1634.
- [71] N. Mohr, C. Kappel, S. Kramer, M. Bros, S. Grabbe, R. Zentel, Targeting cells of the immune system: mannoseylated HPMA-LMA block-copolymer micelles for targeting of dendritic cells, *Nanomedicine* 11 (20) (2016) 2679–2697.
- [72] N. Mohr, M. Barz, R. Forst, R. Zentel, A deeper insight into the post-polymerization modification of polypenta fluorophenyl methacrylates to poly(N-(2-hydroxypropyl) methacrylamide), *Macromol. Rapid Commun.* 35 (17) (2014) 1522–1527.
- [73] Z. Wu, A. Curaj, S. Fokong, E.A. Liehn, C. Weber, T. Lammers, F. Kiessling, M. Zandvoort van, Rhodamine-loaded intercellular adhesion molecule-1-targeted microbubbles for dual-modality imaging under controlled shear stresses, *Circulation, Cardiovasc. imaging* 6 (6) (2013) 974–981.
- [74] F. Heymann, L. Hammerich, D. Storch, M. Bartneck, S. Huss, V. Rüsseler, N. Gassler, S.A. Lira, T. Luedde, C. Trautwein, F. Tacke, Hepatic macrophage migration and differentiation critical for liver fibrosis is mediated by the chemokine receptor C-C motif chemokine receptor 8 in mice, *Hepatology* 55 (3) (2012) 898–909.
- [75] C. Sommer, C. Straehle, U. Koethe, F. Hamprecht, Ilastik: interactive learning and segmentation toolkit, in: *Biomedical Imaging: from Nano to Macro: IEEE International Symposium*, 2011, pp. 230–233.
- [76] F. Gremse, M. Stark, J. Ehling, J.R. Menzel, T. Lammers, F. Kiessling, Imalytics preclinical: interactive analysis of biomedical volume data, *Theranostic* 6 (3) (2016) 328–341.